INSTITUTE OF PHYSICS PUBLISHING JOURNAL OF MICROMECHANICS AND MICROENGINEERING

J. Micromech. Microeng. **14** (2004) 559–566 PII: S0960-1317(04)71039-6

Temperature stabilization of CMOS capacitive accelerometers

Hasnain Lakdawala[1,3] **and Gary K Fedder**[1,2]

[1] Department of Electrical and Computer Engineering, Carnegie Mellon University, 5000 Forbes Ave., Pittsburgh, PA 15213, USA
[2] The Robotics Institute, Carnegie Mellon University, 5000 Forbes Ave., Pittsburgh, PA 15213, USA

Received 27 October 2003
Published 19 January 2004
Online at stacks.iop.org/JMM/14/559 (DOI: 10.1088/0960-1317/14/4/017)

Abstract
CMOS micromachining technology allows the integration of micromachined structures defined by the fine-line geometry of the CMOS interconnect with circuits on the same chip. The mechanical structure is composed of the metal and oxide layers of the CMOS interconnect. One important consideration in design is the control of residual stress difference in the various layers that produce internal bending moments that cause structures to curl in and out of the substrate plane. A temperature stabilization scheme utilizing integrated polysilicon heaters embedded within the micromachined sensor structure to maintain the sensor at a constant temperature has been described. The temperature is maintained higher than the maximum operating temperature of the device. The heated structure is thermally isolated from the substrate to minimize power. This technique has been demonstrated on an out-of-plane accelerometer with a non-linear temperature coefficient of sensitivity. The dc bias stability of the accelerometer improved from 1.7 G $^{\circ}C^{-1}$, to 42 mG $^{\circ}C^{-1}$, and the sensitivity variation reduced from 60% to 18% of the nominal value over a temperature range of 70 °C after temperature control.

(Some figures in this article are in colour only in the electronic version)

1. Introduction

CMOS surface-micromachining technology through conventional foundry-based CMOS processing integrates circuits with mechanical structures at low cost. Circuits can be placed close to the mechanical structures to minimize parasitic effects of long interconnects to sense elements. The material used to define the micromachined sensor is composed of metal layers with interleaved dielectric layers. The possible number of metal and oxide layers used in the mechanical structure is limited only by the number of interconnect levels available in the foundry process. Sensor designs can be exploited to route multiple isolated conductors in microstructures for capacitive sensing. CMOS micromachined sensors based on capacitance sensing have been reported for inertial applications such as accelerometers [1, 2] and gyroscopes [3]. One important issue in the design of such sensors is differences in residual stress in the metal and oxide layers, which produce out-of-plane structural curl. Furthermore, mask misalignments between metal layers during CMOS manufacturing cause in-plane curl [4]. Curl-matching techniques, in which the rotor (moving part) and the stator (stationary part) of the mechanical sensor are designed to have the same curvature, have been used to minimize the impact of residual stress gradients on device performance [1]. However, the stress in each layer is a function of temperature due to the differences in the temperature coefficient of expansion (TCE). This produces changes in in-plane and out-of-plane structural curl with temperature, leading to changes in electrode coupling area and causing variation in sensitivity and dc offset of capacitive sensors.

Oven control temperature stabilization schemes are based on the premise that the effects of temperature on device performance can be eliminated if the device is held at a constant temperature. One method of maintaining a constant

[3] Present address: IC Mechanics Inc, 425 N. Craig St, Pittsburgh, PA 15213, USA.

temperature is heating the device to a temperature greater than its maximum operating temperature. This approach is relatively low cost as it can be implemented using resistive heaters. Heaters to stabilize the frequency by controlling the temperature of devices have been used in commercial high quality quartz resonators[4]. In some cases the device cannot be operated at an elevated temperature and must be controlled to the nominal operating temperature using a combination of heating and cooling. Thermo-electric coolers and heaters are used for temperature control of laser diodes for communication applications. Temperature control of many semiconductor devices is accomplished by setting the temperature of the entire chip to a constant higher temperature using a resistive heater and temperature control circuit integrated along with the package [5]. The heated component has to be thermally isolated to minimize effects on other components placed on the printed circuit board. The power required for heating the chip and the package is high and often requires inclusion of high power driver transistors. This method is expensive to implement, precluding the use of this technique for low-cost sensor applications.

Previously, temperature stabilization schemes have also been applied to micro-devices for various applications. Integrated micro-heaters to stabilize the temperature of surface acoustic wave (SAW) resonators were first proposed by White *et al* [6]. Micro-heaters have been incorporated into film bulk acoustic resonators (FBAR) to improve their temperature performance [7]. Micro-oven temperature control has also been used by researchers to stabilize resonant frequency of CMOS compatible surface-micromachined resonators placed in a vacuum using less than 2 mW of power [8]. Thermal applications of polysilicon microbridges have been investigated, to design flow sensors, pressure sensors and as incandescent light sources [9]. CMOS sensors based on thermal principles have been reported for various applications as well [10].

This paper describes a temperature stabilization scheme for CMOS micromachined z-axis accelerometer, with integrated electronics in which the temperature of the mechanical structure is maintained at a constant temperature, using a micro-oven temperature control scheme. The power consumption and implementation difficulties faced in conventional schemes, have been overcome by limiting the heating to the sensor region. An integrated temperature control scheme transparent to the end user has been implemented. Integrated resistive heaters designed using the polysilicon of the CMOS are located within the device structure to equilibrate its temperature. The change in resistivity of the polysilicon with temperature has been exploited for an *in situ* measurement of the device temperature.

2. CMOS micromachining process

The z-axis accelerometer has been fabricated in a high-aspect-ratio CMOS micromachining process [11]. The process flow, shown in figure 1, illustrates the fabrication of micromachined structures in the Agilent 0.5 μm 3-metal CMOS process used in this work. The mechanical structure is defined using the

[4] Datasheet, Miniature Crystal Oscillator, EX-380, Vectron International, Hudson, NH 0305, USA.

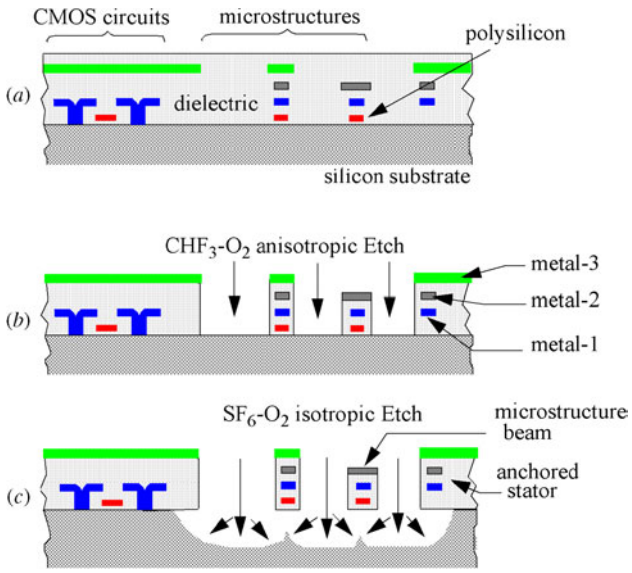

Figure 1. Process flow for the fabrication of micromachined structures in standard CMOS. (*a*) CMOS die from the foundry, (*b*) after anisotropic oxide etch and (*c*) after isotropic silicon etch.

CMOS interconnect layers as masks. The CMOS process is followed by two dry etch steps. The first step is an anisotropic reactive-ion etch (RIE) with CHF_3 and O_2 to etch away oxide not covered by any of the metal layers, resulting in high-aspect-ratio vertical sidewalls. A second isotropic RIE (using SF_6 and O_2) then removes the underlying silicon to release the microstructure. Details of the process are described in [12].

3. CMOS micromachined z-axis accelerometer

A scanning electron micrograph (SEM) of the z-axis accelerometer is shown in figure 2. The accelerometer is a spring–mass system; the force exerted on the mass due to an external acceleration is balanced by a spring force. The suspended structure is attached to a stiff square frame. The spring is designed to be compliant in the z-direction (normal to the substrate), while being stiffer in the x- and y-directions. The spring constants for the spring are $k_z = 0.198$ N m^{-1}, $k_x = 1.93$ N m^{-1} and $k_y = 2.12$ N m^{-1}. The spring is designed using beams with metal-1 and metal-2 interconnect layers of the CMOS process, which are 3.2 μm thick, and made more compliant in the out-of-plane (z) direction by increasing the number of meanders. The increased length of the spring also increases the thermal isolation between the rotor and the stator. The proof mass is designed using all three interconnect metals of the CMOS process stacked to achieve a total plate thickness of 5 μm, which maximizes the mass per unit area. The motion of the mass is detected by a change in the capacitance between the fixed set of stator fingers, and the moving set of comb fingers. The capacitance sense mechanism is sensitive to out-of-plane changes, while rejecting capacitance changes due to in-plane motion. To maximize the sensitivity of the device, the area of the combs is maximized, with 75% of the device area (500 μm $\times$ 500 μm) occupied by comb fingers. The rotor is suspended from a stiff suspended square frame.

In-plane lateral comb drives are commonly used for MEMS capacitance sense and actuation applications [13].

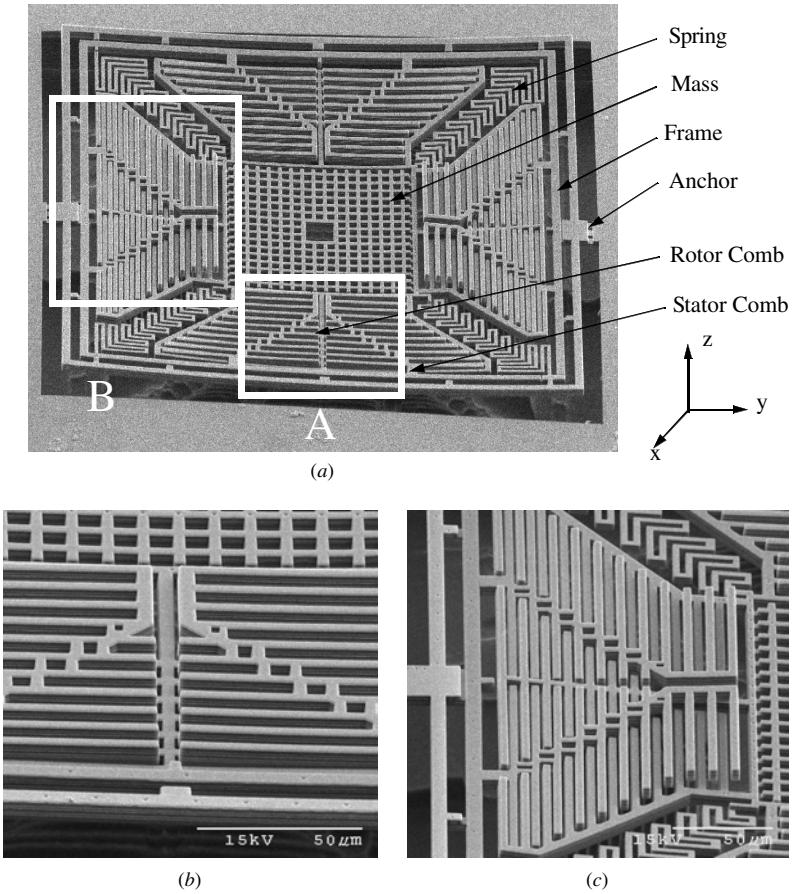

(*a*) (*b*) (*c*)

Figure 2. (*a*) Scanning electron microscope image of the fabricated *z*-axis accelerometer. (*b*) Close up of the comb fingers near the anchor (box A) (*c*) close up of the comb fingers perpendicular to the anchor (box B).

Figure 3(*a*) shows the cross section of the vertical comb drive. All metal layers within comb fingers are tied to the same potential. The curvature of the frame and the rotor are designed to obtain an out-of-plane offset between the rotor and the stator comb fingers. An out-of-plane displacement causes the sidewall overlap area between the combs to change, producing a change in capacitance.

If z_{ov} is the overlap length between the comb fingers, the overall parallel-plate derived capacitance is

$$C_{accn} = \frac{\varepsilon_o z_{ov} L_t}{g_c} \tag{1}$$

where L_t is the total length of all the gaps, and g_c is the separation between the rotor and the stator comb fingers. This simple parallel-plate expression is approximate, since it neglects fringing field effects. Nonetheless it does provide an understanding of the operation of this device. The normalized change in capacitance per unit z displacement is

$$\frac{dC_s}{dz} = \frac{\varepsilon_o L_t}{g_c}. \tag{2}$$

The variation of single comb finger capacitance with out-of-plane displacement simulated using an electrostatic field solver, Raphael[5] is shown in figure 3(*b*). An inherent problem with this comb drive is that the direction of displacement cannot be determined if the rotor and the stator comb fingers are perfectly aligned. This problem is overcome by designing an initial vertical offset between the comb fingers that is larger than the complete range of motion expected for the accelerometer. Residual stress induced curvature of the rotor and the stator is dependent on the particular metal and dielectric layer included in the rotor and stator beams. The structural curl for a given beam cross section is predicted using finite element simulations based on material properties extracted from the test structure data [14]. An iterative finite element simulation for placement of the stator comb attachment to the frame was employed to achieve the best *z*-offset. The SEM in figure 2 shows the structural curl of the rotor relative to the stator. Note that the rotor combs are mostly below the stator combs.

3.1. Capacitance sense circuits

The capacitance sense circuits are placed in the silicon surrounding the device which is at ambient temperature. To ensure that the measured accelerometer sensitivity does not include errors due to circuit temperature characteristic, the circuit gain and offset are made independent of temperature. Chopper-stabilization is used to reduce the flicker noise and temperature drifts of the operational amplifiers. Simplified circuit architecture along with the clock scheme is shown in figure 4. The capacitance bridge, consisting of the device capacitance (C_{accn}) and the reference capacitance (C_r) are

[5] Raphael field solver, Synopsis, Mountain View, CA 94043, USA.

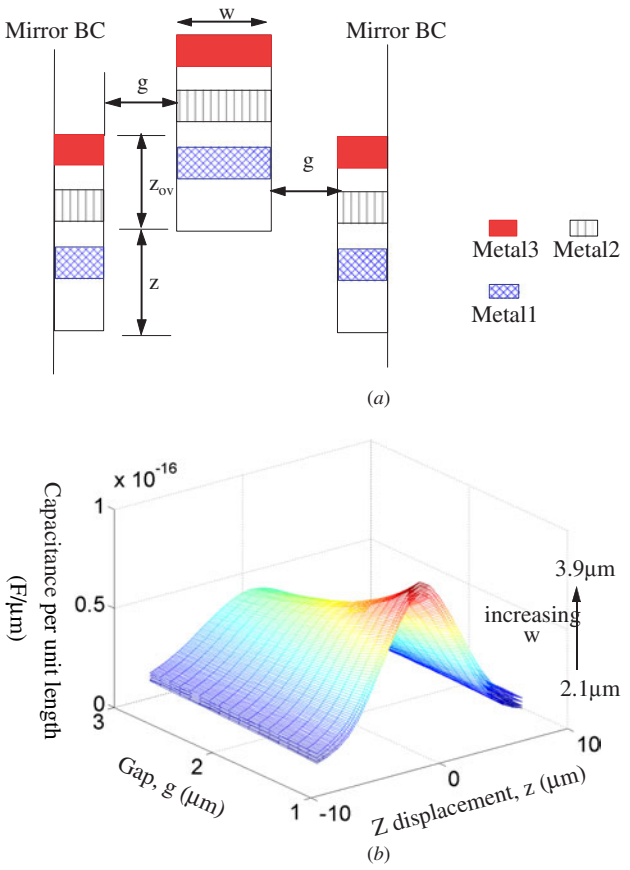

Figure 3. (*a*) Two-dimensional simplified view of the vertical comb drive for electrostatic simulation. (*b*) Variation of the comb finger capacitance with the width (w), the gap (g) and the z displacement.

driven by two signals, V_{modp} and V_{modn}, opposite in phase. These signals are generated by switching dc reference voltages V_{rp} and V_{rn} using non-overlapping clocks ϕ_1 and ϕ_3. V_{modp} is at V_{rp} when ϕ_1 is high, and at V_{rn} when ϕ_3 is high; V_{modn} is at V_{rn} when clock ϕ_1 is high, and V_{rp} when clock ϕ_3 is high. The sense node is reset on a non-overlapping clock ϕ_2 by an n-channel MOS transistor switch, to set a dc voltage. The voltage error introduced by the MOS transistor charge-injection is compensated by introducing an equal and opposite charge injection from a dummy n-channel MOS transistor of half the size and driven by a clock of the opposite phase. The maximum modulation frequency is 1.5 MHz. The gain of the pre-amplifier is set by a ratio of feedback resistors (n_2). The operational amplifier has a NMOS input stage to minimize parasitic capacitance and a folded cascode for increased dc gain. The reduction of parasitic capacitance improves the signal to noise ratio. The demodulator stage consists of a dual input difference amplifier, whose gain is also set by the ratio of two polysilicon resistors. The difference amplifier represented in figure 4, by an operational amplifier with two pairs of inputs consists of a conventional folded cascode operational amplifier with two input stages whose current is summed at the first stage [15]. When ϕ_3 is high, the gain of the difference amplifier is $-(n_2 + 1)$, and when ϕ_1 is high the gain of the amplifier is $(n_2 + 1)$. The output of the circuit after low-pass filtering can

Table 1. Performance summary of the accelerometer.

Parameter	Value
Dimensions	500 μm × 500 μm
Proof mass	200 μm × 200 μm (0.47 μg)
Spring constant (FEA)	$k_z = 0.198$ N m^{-1}
	$k_x = 1.93$ N m^{-1}
	$k_y = 2.12$ N m^{-1}
Natural frequency (z-axis)	5.48 kHz (FEA)
	5.61 kHz (measured)
Sense capacitance	0.193 pF
Sensitivity	130 μV G^{-1}
Noise floor	0.7 mG Hz$^{-1/2}$ at $f = 1.5$ MHz
	3.5 mG Hz$^{-1/2}$ at $f = 140$ kHz
dc voltage variation	-16 mV °C^{-1} or 1.7 G °C^{-1}
Percentage sensitivity variation (30–100 °C)	60%

be written as

$$V_{\text{out}} = \frac{(1-\gamma)(n_1+1)(n_2+1)\Delta C_{\text{accn}}(V_{\text{rp}} - V_{\text{rn}})}{C_{\text{accn}} + C_{\text{r}} + C_{\text{p}}} \tag{3}$$

$$\Delta C_{\text{accn}} = C_{\text{accn}} - C_{\text{r}} \tag{4}$$

where C_{p} is the total parasitic capacitance at the sense node and γ is the duty cycle of the reset clock ϕ_2. ΔC_{accn} is the change in capacitance of the sensor relative to the reference capacitor. An identical z-constrained accelerometer is used as a reference capacitor. This provides a first-order cancellation of thermal effects. Careful attention must be paid to the layout of the circuits to ensure that temperature gradients induced due to the heating of the microstructure do not change resistor ratios and hence affect the temperature coefficient of the circuits. The dc drift of the circuit, without the accelerometer is 170 μV/°C/V (∼18 mG/°C/V), and a negligible change in circuit gain was seen until 104 °C. The bandwidth of the circuit is limited to 1.1 kHz with an off-chip low-pass filter. The dynamic range of the circuit is 3.8 V, which corresponds to about 400 G.

3.2. Characterization of the z-axis accelerometer

The z-axis accelerometer was wire-bonded in a 40 pin DIP package and placed on a Bruel and Kjaer Model 4808 vibration exciter to induce sinusoidal accelerations ranging from 1 G to 10 G. The acceleration of the exciter was simultaneously measured by a reference accelerometer. The nominal sensitivity of the transducer before circuit gain is 0.13 mV/G/V (for $V_{\text{rp}} - V_{\text{rn}} = 1$ V), and 9.3 mV G^{-1} after on-chip amplification. The measured noise floor ranged from 0.7 to 3.5 mG Hz$^{-0.5}$, when the modulation frequency, f, varies from 140 kHz to 1500 kHz. The noise decreases with an increase in the modulation frequency, indicating that the performance of the accelerometer is limited by flicker noise. The cross-axis sensitivity rejection ratio was 32 dB. The mechanical resonant frequency of the accelerometer was 5.61 kHz. The linearized dc offset variation of the accelerometer is 1.7 G °C^{-1}. The total sensitivity variation across a temperature range of 70 °C was about 70% of the nominal value. The performance of the accelerometer is summarized in table 1.

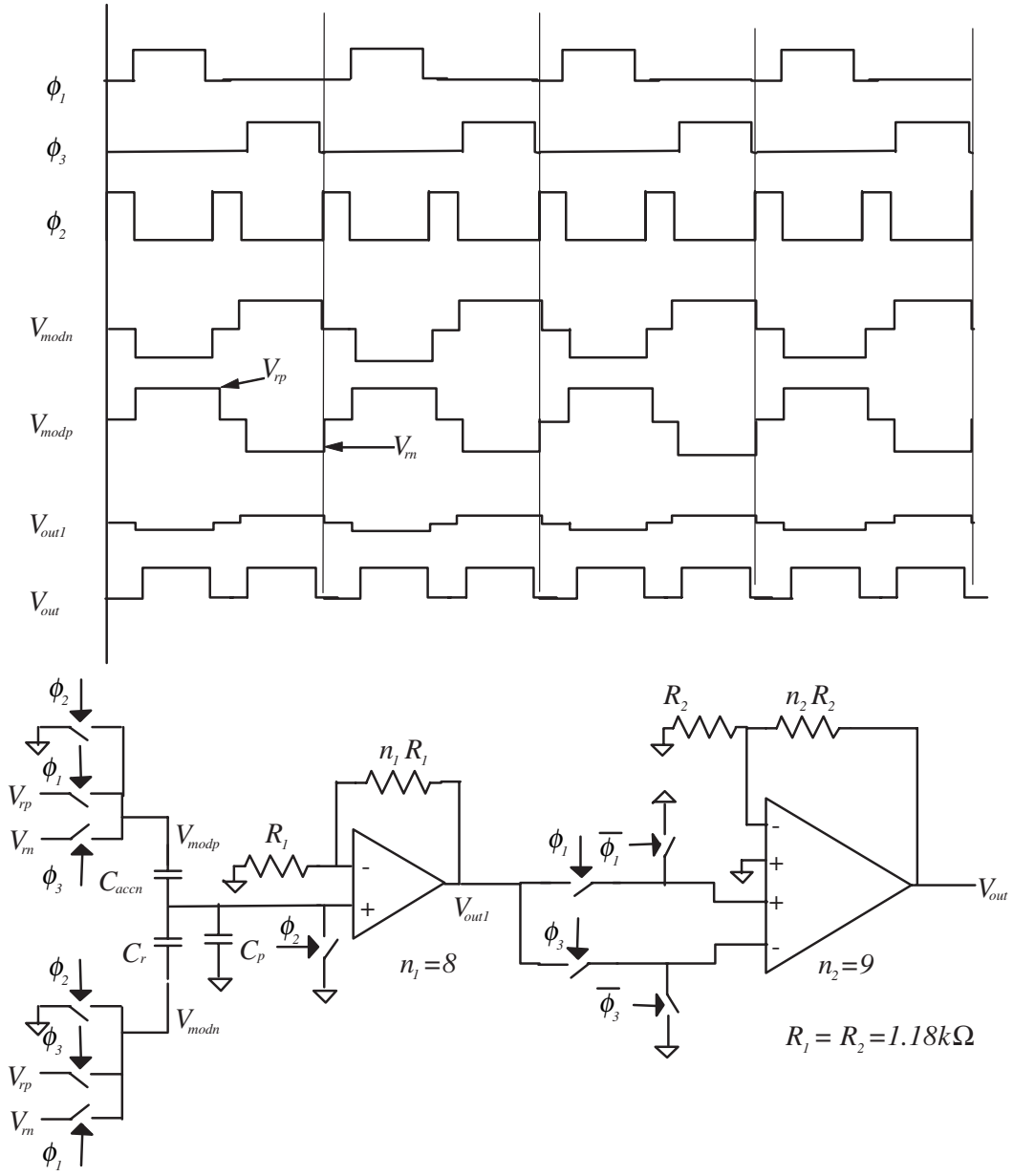

Figure 4. Schematic of the capacitance sense circuits, along with the non-overlapping clock and output signals.

4. Temperature stabilization scheme

To improve the temperature stability of the out-of-plane accelerometer, a micro-oven temperature control scheme was implemented. Ambient temperature changes cause changes in residual stresses that change the relative offset between the rotor and the stator fingers of the accelerometer. The change in the overlap area produces a dc offset change with temperature. The out-of-plane motion due to temperature is indistinguishable from a motion due to acceleration. The sensitivity of the accelerometer, from (3), is a function of the total comb capacitance (C_{accn}), which varies with temperature.

To implement the micro-oven temperature control scheme, the polysilicon layer of the CMOS process is exploited for heater and temperature sensor design. It is the most suitable heater material in the CMOS process due to its high resistivity and melting point [16].

4.1. Integrated heater design

To obtain uniform temperature distribution across the accelerometer, independent heaters are embedded in the stator frame, rotor proof-mass and the rotor comb fingers. The placement of the heaters is shown in figure 5. The average temperature in each of the heaters is set by a constant resistance control scheme. The use of the independent heaters provides greater flexibility to achieve uniform temperature distribution.

The heat loss from the device is dominated by thermal conduction to the substrate through air due to the large surface area and the proximity of the underlying silicon substrate. Heat loss from the anchor regions is minimized by improving the thermal isolation. Thermal isolation of the anchors is increased by minimizing the cross-sectional area and slotting the metal cover [17]. The presence of a

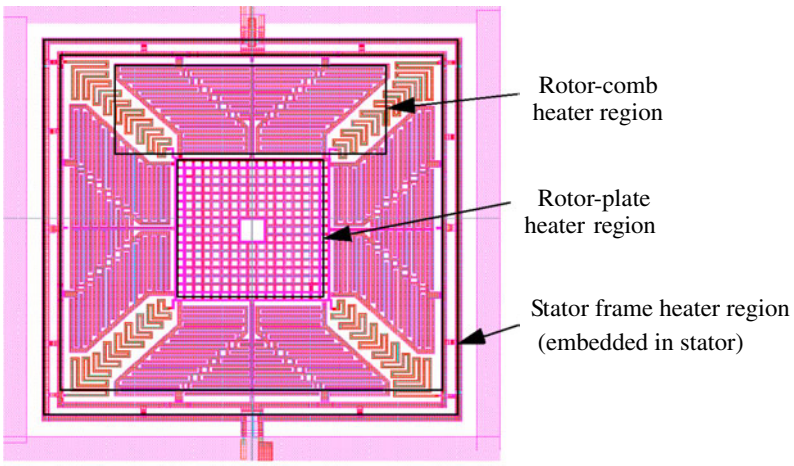

Figure 5. The layout of the accelerometer showing the rotor-plate, stator and the rotor-comb heater regions. The heater consists of embedded polysilicon resistors, designed to provide a uniform heat distribution.

Table 2. Summary of heater control performance.

Parameter	No control	Rotor-plate heater control only	Comb heater control only	Stator heater control only	All heater control
Main heater resistance	–	899 Ω	942 Ω	1470 Ω	–
Zero-G temperature coefficient	1.7 G °C^{-1}	0.46 G °C^{-1}	1.1 G °C^{-1}	76 mG °C^{-1}	−42 mG °C^{-1}
Sensitivity variation (30 °C–104 °C)	60%	37.9%	25.4%	34.5%	17.9%
Heater input power at $T = 30$ °C	0	29.4 mW	64.7 mW	80.7 mW	97.5 mW

temperature gradient across the device is not desirable as the structural curl is then affected by the ambient temperature. The increased thermal isolation at the anchor reduces the temperature gradients within the device, and this improves the temperature uniformity. The dimensions of the polysilicon heaters within the device structure was optimized by a finite difference modelling technique, using thermal properties of the CMOS process [18]. Each beam of the accelerometer was modelled as a thermal-equivalent electrical network and solved in SPICE. The dimensions of each heater were optimized using a modified Levenberg algorithm [19] to obtain the most uniform temperature distribution. The nominal resistance of each resistor is between 0.9 and 1.5 kΩ, to enable design of driver circuits in a 5 V CMOS process. The average temperature of the heaters was monitored from a measurement of the resistance. The polysilicon has a temperature coefficient of resistance (TCR), α, of 0.0049 K^{-1}, with a tolerance of ±10%, as measured in a temperature-controlled oven. The thermal time constant of the device is about 3 ms, which is much smaller than the time constant of changes in ambient temperature change.

4.2. Temperature control

The average temperature of the heater is set by maintaining the heater resistance, R_H, such that,

$$R_H = R_{H0}(1 + \alpha \Delta T) \tag{5}$$

where, R_{H0} is the heater resistance at nominal temperature and ΔT is the temperature increase above the nominal temperature. The chip temperature is measured by an on-chip proportional to absolute temperature (PTAT) circuit. The temperature characteristic of the circuit was calibrated in a temperature-controlled oven using a thermocouple attached to the DIP package. The stator, rotor and the rotor-comb heaters were independently controlled to achieve a uniform distribution across the device. The constant resistance temperature control scheme was implemented using a personal computer (PC) running Labview 5.1 (National Instruments, Austin, TX) and a Keithley source meter (Model 236) linked by GPIB bus. The reference and the device heaters were simultaneously heated to the same temperature. Each heater resistance was kept constant to the value determined by the control temperature. The ambient temperature of the chip was swept using a strip heater attached to the bottom of the package. The test board was mounted on a shaker table with 1 G peak-to-peak acceleration at 230 Hz.

Various temperature control schemes were implemented, to investigate the power performance trade-off and the consequences of non-uniform heating of the device. A summary of the performance of the temperature control schemes is shown in table 2. The zero-G voltage temperature coefficient is defined as the change in dc bias output voltage per degree change in ambient temperature. The sensitivity variation is the ratio of the maximum change in acceleration sensitivity of the accelerometer, over the range of ambient temperature, to the nominal sensitivity. The nominal heater resistance was measured at an ambient temperature of 30 °C. These schemes were:

(1) *Rotor-plate heater control.* The temperature of the rotor-plate heater embedded within the proof mass was controlled at 110 °C. The rotor-comb heaters and the stator heaters were shorted. The temperature profile of the accelerometer is seen in figure 6. There exists a large

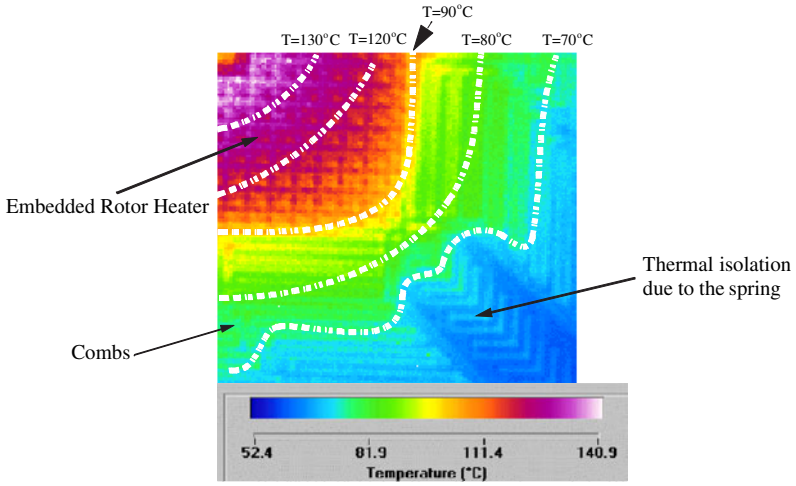

Figure 6. Measured temperature distribution due to rotor heating only, measured by an infrared microscope.

temperature gradient across the stator, consequently the offset and the sensitivity remain temperature dependent.

(2) *Rotor-comb heater control.* The rotor-comb heater was temperature controlled at 110 °C, and the rotor-comb and the stator heaters were shorted. The temperature profile is not uniform due to the heat loss to the unheated stator combs and the rotor.

(3) *Stator heater control.* The stator heater was temperature controlled at 110 °C, and the rotor-comb and the rotor-plate heaters were shorted. Heat loss from the stator to the rotor occurs through the springs and across comb fingers. Since the stator surrounds the structure, the temperature profile is more uniform than the previous two schemes. Consequently, a much lower temperature sensitivity drift is seen.

(4) *Full rotor-plate, rotor-comb and stator control.* In the stator heater control experiment, the rotor heating is significant at lower ambient temperatures due to temperature gradients and the temperature stabilization is not satisfactory. The control of all the heaters within the device ensures that a uniform temperature distribution is generated across the rotor.

Ideally the best performance would be expected when the rotor-plate, stator and the rotor-comb heaters are controlled to be at the same temperature. However, that was not found to be true. When all the heaters were kept at a constant temperature, a negative coefficient of temperature was seen for zero-G dc voltage. This result can be explained by recognizing that the temperature controller can only set the average temperature of the heater resistor. The heater resistor does have higher temperature regions that produce a non-uniform temperature distribution.

The least temperature gradient is obtained from a combination of average temperatures of the stator and the rotor temperatures, with the rotor-comb heater set at the same temperature as the rotor-plate heater. The best performance was measured for a stator temperature of 130 °C, and a rotor temperature of 90 °C. The higher average stator temperature compensates for the heat loss from the anchor point. The zero-G (output when no acceleration is applied) voltage

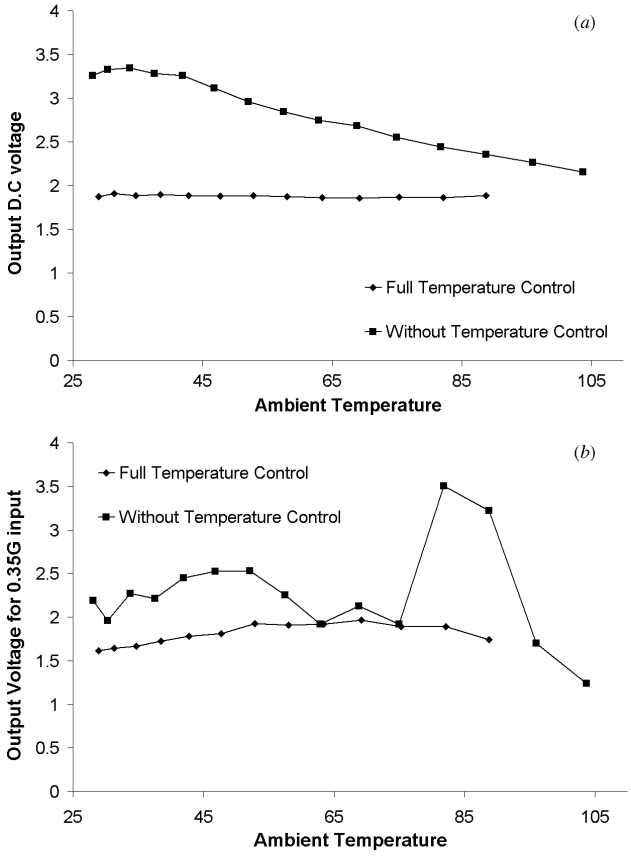

Figure 7. (*a*) The output dc voltage corresponding to a zero-G case. and (*b*) measured RMS voltage for a 0.35 G acceleration input at 330 Hz. The stator is controlled to 130 °C, and the rotor is controlled at 90 °C.

variation with the ambient temperature is shown in figure 7(*a*). The RMS output voltage (with arbitrary gain) measured for a 0.35 G acceleration at 330 Hz is shown in figure 7(*b*). The dc bias or zero-G stability of the accelerometer improved from 1.7 G °C^{-1}, to −42 mG °C^{-1}, and the sensitivity stability improved from 60% to 18% over a temperature range of 70 °C with active temperature control.

5. Discussion

The performance of the temperature control scheme was limited by the ability to achieve a uniform temperature distribution across the device. The heater design optimization helps to improve the temperature distribution across the device, but do not completely eliminate the effect of the temperature gradients. A non-uniform temperature gradient results in the device temperature distribution that is a function of ambient temperature. Another source of error is the mismatch of the TCR of the polysilicon heater material. Differences in the TCR of each heater result in different 'set' temperatures. This leads to temperature gradients in the device that degrade the performance over the ambient temperature of the device. An improvement over the current scheme can be made by integrating the temperature control into a single distributed heater resistor.

The application of temperature control of MEMS sensors using integrated heaters technique is suitable for the stabilization of any sensor with a non-linear temperature response. Circuit-based compensation techniques would require additional calibration and computation circuits, with programmable coefficients. For the accelerometer example, the alignment between the rotor and the stator electrodes is dependent on manufacturing, requiring the gain coefficients of the temperature compensation circuit to be programmed for each device. In lateral sensors, variation due to the in-plane curl induced by mask misalignment during manufacturing can be compensated by this scheme. For example, the temperature stability lateral accelerometer described in [1] is improved by the use of matching rotor and stator curl. Offset variations due to mask misalignments that produce in-plane bending in the springs can be reduced by applying this scheme. The main drawback of the proposed temperature control is the increased power drain, limiting it to applications that can tolerate 20 mW–100 mW of power consumption.

6. Conclusion

We have reported a temperature compensation scheme to improve the performance of a *z*-axis accelerometer, based on micro-oven temperature control of the mechanical structure. The technique leverages layers available in the CMOS process to implement the temperature sense and heating. The placement of the polysilicon heaters embedded in the structural material is independent of the sensor mechanical design. The separation of the mechanical and thermal design parameters allows the integration of this temperature stabilization scheme for other CMOS micromachined sensors.

Acknowledgments

The authors would like to thank X Zhu for the help with release of the devices. This work was partially sponsored by DARPA under the AFRL, Air Force Materiel Command, USAF, under agreements F30602-97-2-0323 and F30602-99-2-0545.

References

[1] Luo H, Zhang G, Carley L R and Fedder G K 2002 A post-CMOS micromachined lateral accelerometer *IEEE/ASME J. Microelectromech. Syst.* **11** 188–95

[2] Xie H and Fedder G K 2002 Vertical comb-finger capacitive actuation and sensing for CMOS-MEMS *Sensors Actuators* A **95** 212–21

[3] Luo H, Fedder G K and Carley L R 2000 An elastically gimbaled Z-axis CMOS-MEMS gyroscopein *Int. Symp. on Smart Structures and Microsystems 2000 (Hong Kong, 19–21 Oct.)*

[4] Iyer S, Lakdawala H, Fedder G K and Mukherjee T 2000 Macromodeling temperature-dependent curl in cmos micromachined beams *4th Int. Conf. on Modeling and Simulation of Microsystems (Hilton Head Island, South Carolina, 19–21 March)*

[5] LM199/LM299/LM399/LM3999 precision voltage reference integrated circuit. Available from National Semiconductor, http://www.national.com

[6] White R M and Goyal R C 1972 Stabilizing surface-wave devices against temperature variations *Electron. Lett.* **8** 142–3

[7] Ruby R and Merchant P 1994 Micromachined thin film bulk acoustic resonators *Proc. 1994 IEEE Int. Frequency Control (Boston, MA)*

[8] Nguyen C T C 1995 Micromechanical resonators for oscillators and filters *Proc. 1995 IEEE Int. Frequency Control (Seattle, WA)*

[9] Mastrangelo C H 1991 Thermal applications of microbridges *PhD Thesis* EECS, U. C. Berkeley

[10] Baltes H, Paul O and Brand O 1998 Micromachined thermally based CMOS microsensors *Proc. IEEE* **86** 1660–78

[11] Fedder G K, Santhanam S, Reed M L, Eagle S C, Guillou D F, Lu M S-C and Carley L R 1996 Laminated high-aspect-ratio microstructures in a conventional CMOS process *Sensors Actuators* A **57** 103–10

[12] Zhu X 2002 Post-CMOS micromachining of surface and bulk structures *PhD Thesis* Department of Electrical and Computer Engineering, Carnegie Mellon University, Pittsburgh, PA

[13] Tang W C, Nguyen T-C H and Howe R T 1989 Laterally driven polysilicon resonant microstructures *Sensors Actuators* **20** 25–32

[14] Lakdawala H and Fedder G K 1999 Analysis of temperature-dependent residual stress gradients in CMOS micromachined structures *Proc. IEEE Int. Conf. on Solid-State Sensors and Actuators (Transducers '99) (Sendai, Japan, 7–10 June 1999)* vol 1 pp 526–9

[15] Lakdawala H 2002 Temperature control of CMOS micromachined sensors *PhD Thesis* Department of Electrical and Computer Engineering, Carnegie Mellon University, Pittsburgh PA, April 2002

[16] Ehmann M, Ruther P, von Arx M, Baltes H and Paul O 2001 Ageing behavior of polysilicon heaters for CMOS microstructures operated at temperatures up to 1200 K *MEMS '01 Interlaken (Switzerland, 21–25 Jan)*

[17] Lakdawala H and Fedder G K 2001 CMOS micromachined infrared imager pixel *Technical Digest of the IEEE Int. Conf. on Solid-State Sensors and Actuators (Munich, Germany, 10–14 June 2001)* pp 1548–51

[18] Von Arx M, Paul O and Baltes H 1995 Determination of the heat capacity of CMOS layers for optimal CMOS sensor design *Sensors Actuators* A **46/47** 428–31

[19] IMSL C library, http://www.vni.com/products/imsl/